Physics-Informed Neural Predictor-Corrector Guidance for Time-Coordinated Reentry of Hypersonic Glide Vehicles

Encheng DAI
PLA Rocket Force University of Engineering
Guangbin Cai
cgb0712@163.com

PLA Rocket Force University of Engineering
Yonghua Fan
Northwestern Polytechnical University
Hui Xu
PLA Rocket Force University of Engineering
Hao Wei
PLA Rocket Force University of Engineering
Yunfei Sun
PLA Rocket Force University of Engineering

Research Article

Keywords: Hypersonic glide vehicle, Physics-informed neural network, Predictor-corrector guidance, Time-coordination guidance

Posted Date: June 23rd, 2026

DOI: https://doi.org/10.21203/rs.3.rs-9996711/v1

Additional Declarations: No competing interests reported.

Physics-Informed Neural Predictor-Corrector Guidance for Time-Coordinated Reentry of Hypersonic Glide Vehicles

Anonymous Author(s)[1]

[1]Anonymous Affiliation, Anonymous Institution, Anonymous.

Abstract

This paper addresses the time-coordinated reentry guidance problem for multiple hypersonic glide vehicles and proposes a physics-informed neural predictor-corrector guidance method. In the proposed framework, the path and terminal constraints are mapped to the bank-angle corridor, and a two-parameter bank-angle magnitude profile is designed in the velocity domain. Combined with heading-angle corridor-based lateral guidance and a cooperative flight-time determination strategy, the method enables rapid online generation of time-coordinated guidance commands. To reduce the computational burden of conventional predictor-corrector guidance, a physics-informed neural predictor is developed to estimate the time-to-go and range-to-go without repeated trajectory propagation. By incorporating energy-domain time- and range-evolution relationships into the training process, the predictor improves both prediction accuracy and physical consistency. Numerical simulations show that the proposed method achieves accurate and adaptive time-coordinated reentry guidance. Compared with numerical integration, the neural predictor requires only about 1.1% of the computational time while maintaining comparable prediction accuracy. Monte Carlo simulations further demonstrate the robustness of the proposed method under initial-state and aerodynamic uncertainties.

Keywords: Hypersonic glide vehicle, Physics-informed neural network, Predictor-corrector guidance, Time-coordination guidance

1 Introduction

With rapid advances in near-space hypersonic glide vehicles (HGV) and reusable aerospace vehicles, conventional guidance designed for an individual flight vehicle is increasingly unable to meet the demands of complex environments. Future aerospace missions are characterized by multiple targets and coupled constraints, which require multiple vehicles to perform cooperative planning and coordinated arrival under limited communication and stringent flight constraints. Therefore, cooperative time-guidance has become an important research topic in aerospace guidance and control, as it directly improves overall mission effectiveness and temporal coordination robustness.

Entry guidance for hypersonic glide vehicles is commonly built around either reference-profile tracking or predictor-corrector guidance. Reference-profile tracking first generates a nominal trajectory or standard flight profile offline and then tracks the prescribed parameters online. This structure is simple and computationally efficient, and it has been widely used in entry and terminal-area energy-management problems. Its performance, however, depends on the quality of the predesigned profile. Changes in the initial state, aerodynamic parameters, atmospheric density, or terminal requirements may require profile redesign, which limits adaptability. Predictor-corrector guidance avoids this dependence by predicting terminal states under candidate control profiles and correcting guidance parameters online. It is better suited to off-nominal conditions and has become a major approach for constrained entry guidance [1–5]. Its main drawback is computational cost: online prediction and correction usually require repeated trajectory propagation, especially in cooperative multi-vehicle missions.

Several studies have extended predictor-corrector guidance to terminal-time control and cooperative arrival. Li et al. [6] proposed a time-coordination entry guidance method for multiple hypersonic vehicles, where lateral guidance provided rough time adjustment and a quadratic bank-angle magnitude profile was corrected in the longitudinal channel. Guo et al. [7] studied terminal-time-control entry guidance based on the quasi-equilibrium glide condition and examined the relation between time-to-go, range-to-go, and terminal velocity. Wang et al. [8] developed a range-determined time-coordination strategy to reduce coupling between time control and motion-form selection. Liang et al. [9] adjusted the heading-error corridor for lateral entry guidance with terminal time constraints. Real-time lateral predictor-corrector guidance has also been extended to terminal heading constraints [10]. Yang et al. [11] derived analytical time-to-go and range-to-go solutions within a three-dimensional corridor for multi-vehicle time-coordinated entry, and Liu et al. [12] proposed a reduced-order terminal-time-constrained entry guidance method. Corridor- and no-fly-zone-constrained studies further show that cooperative entry guidance must handle lateral constraints together with arrival-time coordination [13, 14]. These methods have improved terminal-time control, but numerical predictor-corrector schemes still require repeated high-fidelity integration. Analytical predictors reduce this burden, but often rely on simplified or reduced-order dynamics.

In recent years, data-driven and learning-based methods have provided new possibilities for real-time entry guidance. Neural networks can approximate the nonlinear mapping from flight states and guidance parameters to terminal quantities, replacing repeated trajectory propagation in the guidance loop. Cheng et al. [15] developed a deep-neural-network-based real-time entry guidance method for multi-constrained missions. Li et al. [16] trained a deep learning predictor for the mapping between flight states, bank-profile parameters, range-to-go, and time-to-go in multi-HGV time coordination. Deep reinforcement learning and model-based reinforcement learning have also been applied to hypersonic entry and terminal-time control, where they approximate sequential decision policies under nonlinear dynamics [17–19]. HGV behavior-prediction studies reflect a similar interest in fast trajectory inference [20]. These studies show that learning-based methods can reduce online computational cost and improve guidance autonomy. Purely data-driven predictors, however, may lack physical consistency and can be difficult to interpret [21].

Physics-informed machine learning offers a promising solution to this problem. The basic idea is to embed governing equations, boundary conditions, conservation laws, or other physical relations into the learning process, so that the neural model is not only fitted to data but also regularized by physical knowledge [22–24]. Recent physics-constrained learning further shows that incorporating physical structure can improve data efficiency and interpretability in nonlinear dynamical systems [25]. Physics-informed neural networks (PINN) and related scientific machine learning methods have been widely studied for solving forward and inverse problems governed by differential equations, including neural-operator and high-speed-flow applications [26–29]. However, recent studies also show that naive PINN formulations may suffer from optimization stiffness, imbalanced loss terms, gradient pathologies, and failure modes when the physical residuals are difficult to train or when different loss components have incompatible scales [30, 31]. Recent remedies such as gradient-enhanced residuals, self-adaptive weighting, adaptive sampling, and causal training further indicate that loss balancing and training dynamics are central to reliable PINN deployment [32–35]. These findings are particularly relevant to entry guidance, because the dynamics are highly nonlinear and the prediction targets, such as time-to-go and range-to-go, have different units, scales, and sensitivities. Therefore, when applying physics-informed learning to HGV cooperative guidance, the physical residuals, supervised labels, boundary constraints, slack compensation, and online correction mechanism must be designed in a unified way rather than simply adding a generic differential-equation residual to the loss function.

Motivated by the above gap, this paper develops a physics-informed neural predictor-corrector guidance method for time-coordinated reentry of multiple HGV. The main contributions of this paper are summarized as follows.

1. A bank-angle magnitude profile is designed for longitudinal predictor-corrector guidance. The path and terminal constraints in the altitude–velocity plane are mapped to the admissible boundaries and terminal condition of the bank-angle corridor. A two-parameter profile is then defined in the velocity domain by blending corridor-weighted segments with smooth cubic transition segments. By updating the two shaping parameters to simultaneously regulate the predicted range-to-go and time-to-go, the longitudinal guidance problem is transformed into a bounded two-variable predictor-corrector problem.
2. A physics-informed neural predictor is introduced to avoid repeated trajectory propagation in the guidance loop and to estimate the range-to-go and time-to-go in real time. Rather than relying only on data fitting, the network introduces reentry kinematic relations into the training objective through energy-domain time-consistency residuals, range-evolution residuals, boundary constraints, and penalty

terms for slack variables. This formulation combines supervised fitting with physics-based regularization, leading to better prediction accuracy, physical consistency, and robustness.

3. A cooperative PINN-PCG framework is developed for time-coordinated reentry guidance of multiple HGV. A feasible-arrival-time strategy is used to determine a common arrival-time command that is compatible with vehicles under different initial states. Each vehicle follows this command through neural prediction, longitudinal predictor-corrector updates, and lateral heading-corridor guidance. The framework retains the correction logic and interpretability of conventional PCG, while replacing repeated numerical propagation with neural forward evaluation for real-time cooperative guidance.

2 Problem formulation

2.1 Entry dynamics

A three-degree-of-freedom model over a spherical non-rotating Earth describes the vehicle motion:

$$\begin{cases} \dot{r} = V \sin\gamma \\ \dot{\lambda} = \dfrac{V\cos\gamma\sin\psi}{r\cos\phi} \\ \dot{\phi} = \dfrac{V\cos\gamma\cos\psi}{r} \\ \dot{V} = -D - g\sin\gamma \\ \dot{\gamma} = \dfrac{L\cos\sigma}{V} + \left(\dfrac{V}{r} - \dfrac{g}{V}\right)\cos\gamma \\ \dot{\psi} = \dfrac{L\sin\sigma}{V\cos\gamma} + \dfrac{V\cos\gamma\sin\psi\tan\phi}{r} \end{cases} \tag{1}$$

where r is the geocentric radius; λ is the longitude; ϕ is the latitude; V is the velocity magnitude; γ is the flight-path angle; and ψ is the heading angle. The bank angle is denoted by σ, which determines the direction of the lift vector. g is the gravitational acceleration. For compact notation, the guidance state is written as $\mathbf{x} = [r, \lambda, \phi, V, \gamma, \psi]^T$. The lift and drag accelerations L and D are defined as

$$L = \frac{\rho V^2 S_{\text{ref}} C_L}{2m} \qquad D = \frac{\rho V^2 S_{\text{ref}} C_D}{2m} \tag{2}$$

where S_{ref} is the aerodynamic reference area; m is the vehicle mass; C_L is the lift coefficient; and C_D is the drag coefficient. The atmospheric density ρ is described by the exponential model

$$\rho(h) = \rho_0 \exp\left(-\frac{h}{H_s}\right), \tag{3}$$

where $h = r - R_e$ is the altitude; R_e is the mean Earth radius; ρ_0 is the reference atmospheric density; and H_s is the atmospheric scale height.

2.2 Reentry constraints

The reentry path constraints account for thermal protection, structural safety, and flight feasibility during atmospheric flight. The heating rate, dynamic pressure, and normal load are written as

$$\begin{cases} \dot{Q} = k_Q \sqrt{\rho} V^{3.15} \le \dot{Q}_{\max}, \\ q = \dfrac{1}{2}\rho V^2 \le q_{\max}, \\ n = \dfrac{\sqrt{L^2 + D^2}}{g_0} \le n_{\max}, \end{cases} \tag{4}$$

where $\dot{Q}_{\max}$ is the allowable upper bound of heat rate; $q_{\max}$ is the allowable upper bound of dynamic pressure; $n_{\max}$ is the allowable upper bound of aerodynamic overload; and k_Q is the heat-rate constant.

The bank angle is selected as the main control variable. To account for actuator limits and guidance feasibility, the bank angle and its rate are constrained by

$$\begin{cases} \sigma_{\min} \le \sigma \le \sigma_{\max} \\ |\dot{\sigma}| \le \dot{\sigma}_{\max} \end{cases} \tag{5}$$

where $\sigma_{\min}$ is the lower bound of the bank angle; $\sigma_{\max}$ is the upper bound of the bank angle; and $\dot{\sigma}_{\max}$ is the maximum allowable bank-angle rate.

The terminal constraints are imposed on the terminal altitude, terminal velocity, terminal range-to-go, and terminal arrival time. For time-coordinated guidance, each vehicle is required to reach the terminal condition within a prescribed tolerance of the coordinated arrival time t_c. The terminal constraints are expressed as

$$\begin{cases} |h(t_f) - h_f| \le \varepsilon_h \\ |V(t_f) - V_f| \le \varepsilon_V \\ |S(t_f) - S_f| \le \varepsilon_S \\ |t_f - t_c| \le \varepsilon_t \end{cases} \tag{6}$$

where t_f denotes the actual terminal time; t_c is the prescribed coordinated arrival time; h_f is the desired terminal altitude; V_f is the desired terminal velocity; S_f is the desired terminal range-to-go; ε_h is the allowable altitude tolerance; ε_V is the allowable velocity tolerance; ε_S is the allowable range-to-go tolerance; and ε_t is the allowable arrival-time tolerance.

3 Cooperative time-guidance method

The overall procedure of the proposed cooperative PINN-PCG method is shown in Fig. 1. The framework consists of an offline PINN predictor construction stage and an online cooperative guidance loop. In the offline stage, sampled reentry trajectories are used to train a physics-informed predictor for time-to-go and range-to-go estimation.

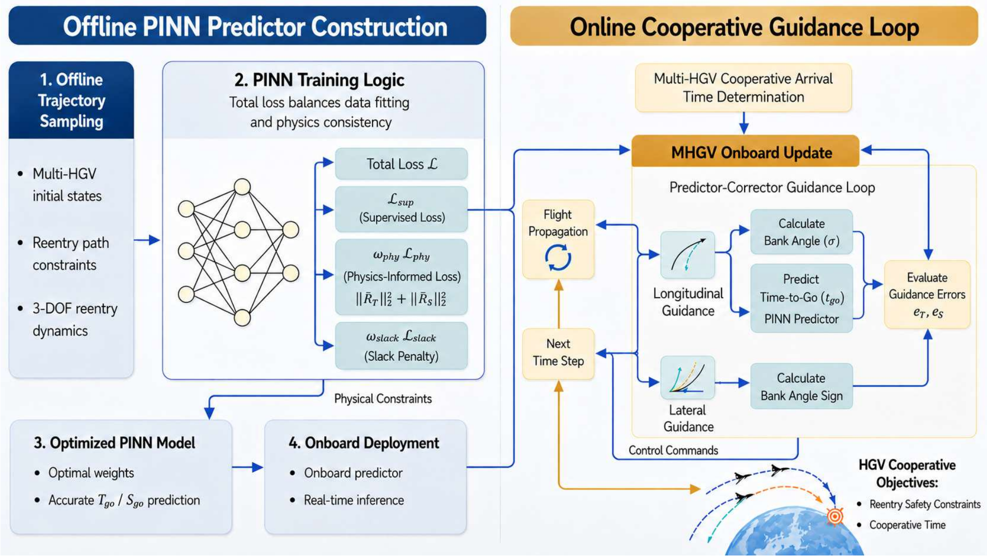

Fig. 1 Overall workflow of the proposed cooperative PINN-PCG method.

In the online stage, the trained predictor is embedded into the predictor-corrector guidance loop to update the bank-angle command for each vehicle under a common arrival-time requirement.

3.1 Longitudinal predictor-corrector guidance

The longitudinal guidance law regulates the remaining range and flight time by shaping the bank-angle magnitude. The path constraints are first converted into an admissible bank-angle corridor. Because the heating rate, dynamic pressure, and normal load depend on altitude and velocity, their limiting values can be mapped into the altitude-velocity plane. With the atmospheric model in Eq. (3), these limiting conditions are

$$\begin{cases} \rho_{\dot{Q}}(V) = \left(\dfrac{\dot{Q}_{\max}}{k_Q V^{3.15}}\right)^2 \\ \rho_q(V) = \dfrac{2q_{\max}}{V^2} \\ \rho_n(V) = \dfrac{2mg_0 n_{\max}}{V^2 S_{\text{ref}}\sqrt{C_L^2 + C_D^2}} \end{cases} \tag{7}$$

where $\rho_{\dot{Q}}(V)$ is the maximum allowable atmospheric density imposed by the heat-rate constraint; $\rho_q(V)$ is the maximum allowable atmospheric density imposed by the dynamic-pressure constraint; and $\rho_n(V)$ is the maximum allowable atmospheric density imposed by the load-factor constraint.

The corresponding altitude boundary for each constraint is obtained as

$$h_c(V) = -H_s \ln\left(\frac{\rho_c(V)}{\rho_0}\right), \qquad c \in \{\dot{Q}, q, n\} \tag{8}$$

where $h_c(V)$ is the minimum admissible altitude for constraint c; and $\rho_c(V)$ represents the corresponding density limit. These boundaries define the feasible reentry corridor in the altitude-velocity plane.

The quasi-equilibrium glide condition converts each altitude-velocity boundary into a bank-angle boundary. When the flight-path angle and its rate remain small during glide, the longitudinal force balance gives

$$L(h, V)\cos\sigma + \frac{V^2}{r} - g = 0 \tag{9}$$

where $L(h, V)$ is the lift acceleration evaluated at altitude h and velocity V. For a given boundary altitude $h_c(V)$, the corresponding bank angle is

$$\sigma_c(V) = \arccos\left(\frac{g(h_c) - V^2/r_c}{L(h_c, V)}\right) \tag{10}$$

where $r_c = R_e + h_c(V)$. The result is clipped to the allowable interval of the bank angle. The bank-angle corridor is defined by its upper and lower boundaries as

$$\begin{cases} \sigma_{\max}^{\text{cor}}(V) = \min\left\{\sigma_{\dot{Q}}(V), \sigma_q(V), \sigma_n(V), \sigma_{\max}\right\} \\ \sigma_{\min}^{\text{cor}}(V) = \sigma_{\min} \end{cases} \tag{11}$$

where $\sigma_{\max}^{\text{cor}}(V)$ is determined by the most restrictive boundary among the heating-rate, dynamic-pressure, load-factor, and maximum bank-angle limits; and $\sigma_{\min}^{\text{cor}}(V)$ is set as a prescribed minimum bank-angle magnitude. As long as the bank-angle magnitude remains inside this corridor, the trajectory is guided to satisfy the major reentry path constraints.

The angle of attack is not treated as an online correction variable in the longitudinal guidance loop. Instead, it is scheduled with velocity by a prescribed law [36]:

$$\alpha(V) = \begin{cases} \alpha_{\max}, & V_{\alpha 1} < V \leq V_0, \\ \dfrac{\alpha_g - \alpha_{\max}}{V_{\alpha 2} - V_{\alpha 1}}(V - V_{\alpha 1}) + \alpha_{\max}, & V_{\alpha 2} < V \leq V_{\alpha 1}, \\ \alpha_g, & V_f < V \leq V_{\alpha 2}. \end{cases} \tag{12}$$

where V_0 is the entry velocity; V_f is the terminal velocity; $\alpha_{\max}$ is the upper bound of the angle of attack; α_g denotes the angle of attack associated with the maximum lift-to-drag ratio; $V_{\alpha 1}$ is the first prescribed switching velocity; and $V_{\alpha 2}$ is the second prescribed switching velocity.

The bank-angle magnitude profile is parameterized in the velocity domain by two normalized shaping parameters $\mathbf{w} = [w_1, w_2]^T \in [0,1]^2$. The prescribed velocity nodes $V_0 > V_1 > V_2 > V_3 > V_f$ divide the profile into several segments. The terminal bank-angle magnitude σ_f is obtained from the quasi-equilibrium glide condition at the prescribed terminal altitude and velocity.

The bank-angle magnitude profile is defined as

$$\sigma_m(V; \mathbf{w}) = \begin{cases} w_1\sigma_{\min} + (1 - w_1)\sigma_{\max}^{\text{cor}}(V), & V_1 < V \le V_0, \\ \mathcal{B}_{12}(V; \mathbf{w}), & V_2 < V \le V_1, \\ w_2\sigma_{\min} + (1 - w_2)\sigma_{\max}^{\text{cor}}(V), & V_3 < V \le V_2, \\ \mathcal{B}_{3f}(V; \mathbf{w}), & V_f \le V \le V_3, \\ \sigma_f, & V < V_f. \end{cases} \tag{13}$$

where $\mathcal{B}_{12}(\cdot)$ is the cubic B-spline transition segment between V_1 and V_2; and $\mathcal{B}_{3f}(\cdot)$ is the cubic B-spline transition segment between V_3 and V_f. Both transition segments are expressed in Bezier form. The segment $\mathcal{B}_{12}(\cdot)$ joins the magnitude set by w_1 at V_1 to that set by w_2 at V_2. The segment $\mathcal{B}_{3f}(\cdot)$ joins the magnitude set by w_2 at V_3 to the terminal value σ_f at V_f. The complete profile therefore uses only the two adjustable parameters w_1 and w_2 to correct remaining range and flight time.

For a generic transition interval between two endpoint velocities V_a and V_b, the cubic transition segment is written as

$$\mathcal{B}(V) = (1 - \eta)^3 P_0 + 3(1 - \eta)^2 \eta P_1 + 3(1 - \eta)\eta^2 P_2 + \eta^3 P_3, \tag{14}$$

where the normalized velocity coordinate is defined as

$$\eta = \frac{V - V_a}{V_b - V_a}. \tag{15}$$

where P_0–P_3 are the control points of the local transition segment. The endpoint control points follow from the bank-angle magnitudes of the adjacent segments, and the internal points are selected from the endpoint slopes of the precomputed bank-angle corridor. This construction gives smooth transitions between adjacent segments without adding online optimization variables.

The signed bank-angle command is formed by combining the bank-angle magnitude from longitudinal guidance with the bank-sign variable generated by lateral guidance and is written as

$$\sigma_{\text{cmd}}(t) = b(t)\sigma_m(V; \mathbf{w}), \qquad b(t) \in \{-1, 1\} \tag{16}$$

The parameters w_1 and w_2 provide two degrees of freedom for longitudinal correction. A smaller bank-angle magnitude increases the vertical lift component and generally enlarges the achievable range and flight time. A larger magnitude reduces the vertical lift component and shortens the trajectory. The two-parameter profile can therefore correct remaining range and flight time at the same guidance update.

At each guidance update, the prescribed coordinated arrival time t_c defines the commanded remaining flight time as

$$T_{\text{cmd}}(t) = t_c - t. \tag{17}$$

The required range-to-go is computed from the current great-circle range to the target as

$$S_{\text{req}}(t) = S_{\text{togo}}(t) - S_f \tag{18}$$

where S_{togo} is the great-circle range to the target; and S_f is the desired terminal residual range. For a given parameter vector $\mathbf{w}$, the trajectory predictor propagates the vehicle dynamics with the bank-angle profile in Eq. (13) until the terminal energy condition is reached. It returns the remaining flight time and accumulated remaining range:

$$[T_{\text{pre}}(\mathbf{x}, \mathbf{w}), S_{\text{pre}}(\mathbf{x}, \mathbf{w})]^T = \mathcal{P}(\mathbf{x}, \mathbf{w}) \tag{19}$$

The longitudinal correction residual is defined as

$$\mathbf{r}(\mathbf{w}) = \begin{bmatrix} S_{\text{pre}}(\mathbf{x}, \mathbf{w}) - S_{\text{req}} \\ T_{\text{pre}}(\mathbf{x}, \mathbf{w}) - T_{\text{cmd}} \end{bmatrix} \tag{20}$$

The online correction drives both components of $\mathbf{r}(\mathbf{w})$ toward zero, so that the predicted trajectory satisfies the required range and coordinated arrival time. The bank-angle profile correction is formulated as the bound-constrained least-squares problem

$$\begin{aligned} \min_{\mathbf{w}} \quad & \frac{1}{2} \|\mathbf{r}(\mathbf{w})\|_2^2 , \\ \text{s.t.} \quad & \mathbf{0} \le \mathbf{w} \le \mathbf{1}. \end{aligned} \tag{21}$$

A damped Gauss-Newton scheme updates the bank-angle profile parameters. The residual sensitivity matrix is

$$J(\mathbf{w}) = \frac{\partial \mathbf{r}}{\partial \mathbf{w}}. \tag{22}$$

Because the residual is evaluated through trajectory prediction, the numerical predictor-corrector implementation computes the sensitivity matrix by finite differences. A regularized Gauss-Newton correction improves numerical robustness:

$$\Delta \mathbf{w} = -\left(J^T J + \mu I\right)^{-1} J^T \mathbf{r}, \tag{23}$$

where μ is the Gauss-Newton damping coefficient. The parameter vector is then updated with a line-search step and projected onto the feasible set:

$$\mathbf{w}^{k+1} = \mathbf{w}^k + \beta \Delta \mathbf{w} \tag{24}$$

where β is the line-search step size. This iterative correction is performed at each guidance update, and the resulting profile parameters generate the current longitudinal bank-angle command.

3.2 Lateral predictor-corrector guidance

The lateral guidance law determines the bank-sign variable $b(t)$, while the longitudinal guidance law provides the bank-angle magnitude. A heading-corridor method keeps the vehicle heading within a prescribed corridor around the target line-of-sight direction. The current bank sign is retained when the heading error remains inside the corridor. Once the error exceeds the corridor boundary, the bank sign is updated to drive the heading back toward the corridor center.

The target longitude is denoted by λ_T; and the target latitude is denoted by ϕ_T. The line-of-sight azimuth is computed as

$$\psi_{\text{LOS}} = \text{atan2}\left(\sin(\lambda_T - \lambda), \cos\phi \tan\phi_T - \sin\phi\cos(\lambda_T - \lambda)\right) \tag{25}$$

To allow a larger lateral correction margin in the high-speed phase and a tighter terminal alignment requirement in the low-speed phase, the maximum allowable heading error is defined as a velocity-dependent piecewise linear function:

$$\Delta\psi_{\text{cor}}(V) = \begin{cases} \Delta\psi_{\text{cor},1}, & V_{\psi 1} < V \leq V_0 \\ \dfrac{\Delta\psi_{\text{cor},2} - \Delta\psi_{\text{cor},1}}{V_{\psi 2} - V_{\psi 1}}(V - V_{\psi 1}) + \Delta\psi_{\text{cor},1}, & V_{\psi 2} < V \leq V_{\psi 1} \\ \Delta\psi_{\text{cor},2}, & V_f < V \leq V_{\psi 2} \end{cases} \tag{26}$$

where $\Delta\psi_{\text{cor},1}$ is the prescribed maximum heading error in the high-speed region; $\Delta\psi_{\text{cor},2}$ is the prescribed maximum heading error in the low-speed region; $V_{\psi 1}$ is the first transition velocity of the heading corridor; and $V_{\psi 2}$ is the second transition velocity of the heading corridor. This piecewise definition provides a wide heading corridor at high speed and gradually tightens the corridor as the vehicle approaches the terminal phase. The bank-sign update law is then given by

$$b^k = \text{sign}(\sigma^k) = \begin{cases} -1, & \Delta\psi > \Delta\psi_{\text{up}} \\ 1, & \Delta\psi < \Delta\psi_{\text{down}} \\ \text{sign}(\sigma^{k-1}), & \Delta\psi_{\text{down}} \leq \Delta\psi \leq \Delta\psi_{\text{up}} \end{cases} \tag{27}$$

where $\Delta\psi$ denotes the heading error; $\Delta\psi_{\text{up}}$ represents the upper boundary of the heading corridor; $\Delta\psi_{\text{down}}$ represents the lower boundary of the heading corridor; b^k denotes the bank-sign variable at the kth guidance cycle; σ^k refers to the bank angle at the kth guidance cycle; and $\text{sign}(\sigma^{k-1})$ gives the bank sign from the previous guidance cycle.

3.3 Physics-Informed Neural-Network-Assisted Longitudinal Guidance

In conventional predictor-corrector guidance, the remaining range and time-to-go must be evaluated repeatedly for different bank-angle profile parameters. Numerical propagation gives reliable predictions, but it requires multiple integrations at each guidance update. This cost can lengthen the correction period and limit real-time performance.

Analytical approximations are faster, but their accuracy can degrade under nonlinear dynamics, path constraints, and off-nominal conditions. The present method uses a physics-informed neural predictor to estimate remaining flight time and remaining range in real time.

The training dataset is generated offline from 10,000 randomly sampled trajectories. The initial states are perturbed around their nominal values, and the bank-profile parameters w_1 and w_2 are sampled uniformly. For each case, the bank-angle profile $\sigma_m(V;\mathbf{w})$ is fixed, and the vehicle dynamics are propagated with a fourth-order Runge-Kutta method until the terminal-energy condition is reached. Along each trajectory, 100 points are sampled uniformly, giving approximately 1.0×10^6 supervised samples. The dataset is divided into training, validation, and testing subsets at a ratio of 8:1:1. All input and output variables are standardized before training. The same parameter vector $\mathbf{w} = [w_1, w_2]^T$ is used in the numerical predictor and the neural predictor.

At each guidance update, the input feature vector is constructed from the current flight state, target-relative geometry, and bank-angle profile parameters. To avoid redundant energy-related information, the energy variable is not included as a network input. The feature vector is defined as

$$\mathbf{z} = \left[\frac{h}{H_{\text{ref}}}, \frac{V}{V_{\text{ref}}}, \gamma, \sin\phi, \cos\phi, \frac{S_{\text{togo}}}{R_e}, \sin e_\psi, \cos e_\psi, w_1, w_2\right]^T \tag{28}$$

where H_{ref} is the altitude normalization constant; V_{ref} is the velocity normalization constant; S_{togo} is the current great-circle range to the target; e_ψ is the heading error relative to the target line of sight; w_1 is the first shaping parameter of the bank-angle magnitude profile; and w_2 is the second shaping parameter of the bank-angle magnitude profile.

The neural predictor estimates the time-to-go and the remaining range as

$$\left[\hat{T}_{\text{go}}, \hat{S}_{\text{go}}\right]^T = f_\theta(\mathbf{z}) \tag{29}$$

where $f_\theta(\cdot)$ denotes the trained physics-informed neural network.

The network is not trained as a purely data-driven regressor. Physical information enters through energy-domain time consistency and range-evolution consistency. The supervised data loss is

$$\mathcal{L}_{\text{sup}} = \left\|\hat{T}_{\text{go}} - T_{\text{go}}\right\|_2^2 + \left\|\hat{S}_{\text{go}} - S_{\text{go}}\right\|_2^2 \tag{30}$$

where T_{go} is the time-to-go reference label obtained from the numerical predictor; and S_{go} is the range-to-go reference label obtained from the numerical predictor.

The time-related physical constraint is derived from the monotonic energy dissipation during reentry flight. The specific mechanical energy is defined as

$$E = \frac{V^2}{2} - \frac{\mu}{r} \tag{31}$$

where μ denotes the gravitational parameter. Although E is not used as an input feature, it is computed from the current flight state when the physical residual is evaluated. Under the non-rotating point-mass dynamics, the time derivative of E satisfies

$$\dot{E} = -DV \tag{32}$$

Since the remaining flight time decreases along the trajectory, the energy-domain time consistency relation is written as

$$\frac{d\hat{T}_{\mathrm{go}}}{dE} = \frac{1}{-\dot{E}} \tag{33}$$

The corresponding time physical residual is defined as

$$R_T = \frac{d\hat{T}_{\mathrm{go}}}{dE} - \frac{1}{-\dot{E}} \tag{34}$$

The range-related physical constraint follows from the evolution of the remaining range. The remaining range should decrease with the ground-speed component along the target line-of-sight direction:

$$\frac{d\hat{S}_{\mathrm{go}}}{dt} + V_g = 0 \tag{35}$$

where the line-of-sight projected ground speed is given by

$$V_g = \frac{R_e}{r} V \cos\gamma \cos\left(\psi - \psi_{\mathrm{LOS}}\right) \tag{36}$$

The range physical residual is then defined as

$$R_S = \frac{d\hat{S}_{\mathrm{go}}}{dt} + V_g \tag{37}$$

Slack variables are introduced to reduce the effect of model mismatch on the physical regularization. The slack-augmented residuals are

$$\tilde{R}_T = R_T + s_T, \qquad \tilde{R}_S = R_S + s_S \tag{38}$$

where s_T is the time-residual slack variable generated by the auxiliary slack head; and s_S is the range-residual slack variable generated by the auxiliary slack head. They provide limited compensation for aerodynamic uncertainty, atmospheric variation, and modeling simplifications. To prevent the slack variables from replacing the physical constraints, they are penalized during training:

$$\mathcal{L}_{\mathrm{slack}} = \|s_T\|_2^2 + \|s_S\|_2^2 \tag{39}$$

The physics-informed loss is written as

$$\mathcal{L}_{\text{phy}} = \left\| \tilde{R}_T \right\|_2^2 + \left\| \tilde{R}_S \right\|_2^2 \tag{40}$$

The total training loss is defined as

$$\mathcal{L} = \mathcal{L}_{\text{sup}} + \omega_{\text{phy}}\mathcal{L}_{\text{phy}} + \omega_{\text{slack}}\mathcal{L}_{\text{slack}} \tag{41}$$

where ω_{phy} is the weighting coefficient of the physical residual loss; and ω_{slack} is the weighting coefficient of the slack penalty. During online guidance, $\hat{T}_{\text{go}}$ and $\hat{S}_{\text{go}}$ are used for longitudinal correction.

3.4 Cooperative arrival-time determination

For multi-vehicle cooperative reentry guidance, a common arrival time is selected before flight and assigned to all vehicles as the terminal-time command. For the ith vehicle, the feasible arrival-time interval is

$$\mathcal{T}_i = [t_{i,\min}, t_{i,\max}] \tag{42}$$

where $t_{i,\min}$ is the minimum feasible arrival time of the ith vehicle; and $t_{i,\max}$ is the maximum feasible arrival time of the ith vehicle. The interval $\mathcal{T}_i$ is obtained by scanning the commanded terminal time and checking whether the terminal and path constraints can be satisfied.

The common arrival time must lie in the intersection of all feasible intervals. The common feasible interval is

$$\mathcal{T}_{\text{co}} = \bigcap_{i=1}^{N} \mathcal{T}_i = \left[\max_i t_{i,\min}, \min_i t_{i,\max}\right] \tag{43}$$

A feasible cooperative arrival time exists when $\max_i t_{i,\min} \leq \min_i t_{i,\max}$. The midpoint of this interval is selected to avoid a boundary command:

$$t_{\text{co}} = \frac{1}{2}\left(\max_i t_{i,\min} + \min_i t_{i,\max}\right). \tag{44}$$

The selected t_{co} is then assigned to each vehicle as the coordinated arrival-time command.

During online guidance, the corresponding time and range errors are defined as

$$e_{T,i} = \hat{T}_{\text{go},i} - T_{\text{cmd},i}, \qquad e_{S,i} = \hat{S}_{\text{go},i} - S_{\text{req},i}. \tag{45}$$

where $T_{\text{cmd},i}(t)$ denotes the commanded remaining time; and $S_{\text{req},i}(t)$ denotes the required remaining range.

The predictor-corrector module updates the bank-profile parameters according to $e_{T,i}$ and $e_{S,i}$, reducing the remaining-time and remaining-range errors together.The

Algorithm 1 Online cooperative PINN-PCG guidance procedure

Require: Initial states $\mathbf{x}_{i,0}$, target position, trained predictor f_θ, path constraints, terminal tolerances
Ensure: Bank-angle command $\sigma_{\mathrm{cmd},i}$ for each vehicle

```
Determine 𝒯_i = [t_{i,min}, t_{i,max}] for each vehicle and compute t_co from Eq. (44)
Set the coordinated arrival-time command as t_c = t_co
for each vehicle i = 1, ..., N do
    Initialize the bank-profile parameters w_i = [w_{1,i}, w_{2,i}]^T
end for
while the terminal conditions are not satisfied do
    for each vehicle i = 1, ..., N do
        Update the current state x_i(t) and target-relative geometry
        Construct the PINN input vector z_i from x_i(t), target-relative quantities, and w_i
        Predict [T̂_{go,i}, Ŝ_{go,i}]^T = f_θ(z_i)
        Form e_{T,i} and e_{S,i} from Eq. (45)
        Update w_i by the regularized predictor-corrector correction
        Generate the longitudinal bank-angle magnitude σ_{m,i}(V; w_i)
        Determine the bank-sign variable b_i from lateral guidance
        Apply the command σ_{cmd,i} = b_i σ_{m,i}(V; w_i)
    end for
end while
```

Table 1 Main simulation parameters

Parameter	Symbol	Value
Mass	m	907 kg
Reference area	S_{ref}	0.48 m^2
Maximum heating rate	$\dot{Q}_{\max}$	1500 kW/m^2
Maximum dynamic pressure	$q_{\max}$	100 kPa
Maximum normal load	$n_{\max}$	3.0
Maximum bank angle	$\sigma_{\max}$	85 deg
Minimum bank angle	$\sigma_{\min}$	0 deg
Maximum bank-angle rate	$\dot{\sigma}_{\max}$	25 deg/s

vehicles are guided toward the terminal region at approximately t_{co} while satisfying their own terminal and path constraints.

The complete online implementation of the proposed cooperative PINN-PCG method is summarized in Algorithm 1. The algorithm emphasizes the closed-loop information flow from state measurement, neural prediction, longitudinal correction, lateral sign selection, and bank-angle command generation.

4 Simulation

Numerical simulations are used to evaluate the proposed physics-informed neural-network-assisted guidance method. The CAV-H vehicle model serves as the simulation platform, and the main parameters are summarized in Table 1.

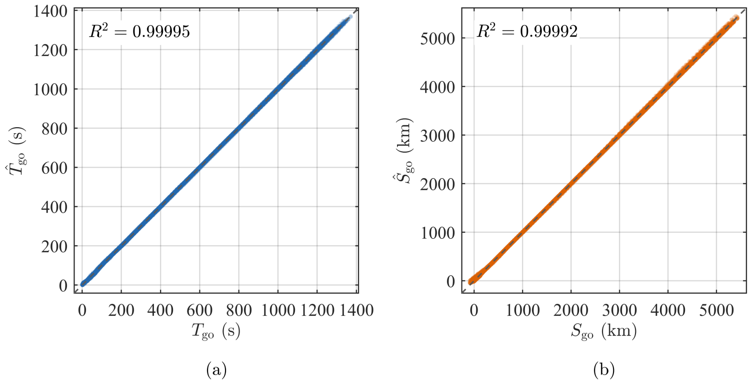

Fig. 2 Predicted-versus-reference results of the proposed physics-informed predictor: (a) remaining flight time T_{go}; (b) remaining flight range S_{go}.

4.1 Evaluation of the Physics-Informed Neural Predictor

4.1.1 Prediction Accuracy

The prediction accuracy of the proposed neural predictor is evaluated on the independent test set. The input of the network is the normalized guidance state and bank-profile parameter vector, while the predicted outputs are the remaining flight time $\hat{T}_{go}$ and the remaining range $\hat{S}_{go}$. The prediction performance is measured by the root mean square error (RMSE) and the coefficient of determination R^2, which are defined as

$$\text{RMSE} = \sqrt{\frac{1}{N_{\text{test}}} \sum_{j=1}^{N_{\text{test}}} (\hat{y}_j - y_j)^2}, \tag{46}$$

$$R^2 = 1 - \frac{\sum_{j=1}^{N_{\text{test}}} (y_j - \hat{y}_j)^2}{\sum_{j=1}^{N_{\text{test}}} (y_j - \bar{y})^2}. \tag{47}$$

where N_{test} denotes the number of test samples; y_j is the reference value obtained from the test data; $\hat{y}_j$ is the corresponding predicted value of the neural predictor; and $\bar{y}$ is the mean value of the reference data. For the remaining-flight-time prediction, y_j corresponds to T_{go}; and $\hat{y}_j$ corresponds to $\hat{T}_{go}$. For the remaining-range prediction, y_j corresponds to S_{go}; and $\hat{y}_j$ corresponds to $\hat{S}_{go}$. A smaller RMSE indicates a lower prediction error, while an R^2 value closer to one indicates better agreement between the predicted values and the reference data.

The test-set prediction results are shown in Figs. 2 and 3. The predicted-versus-reference plots in Fig. 2 place most samples close to the diagonal for both T_{go} and S_{go}. The error histograms in Fig. 3 are centered near zero, indicating little systematic bias on the test set.

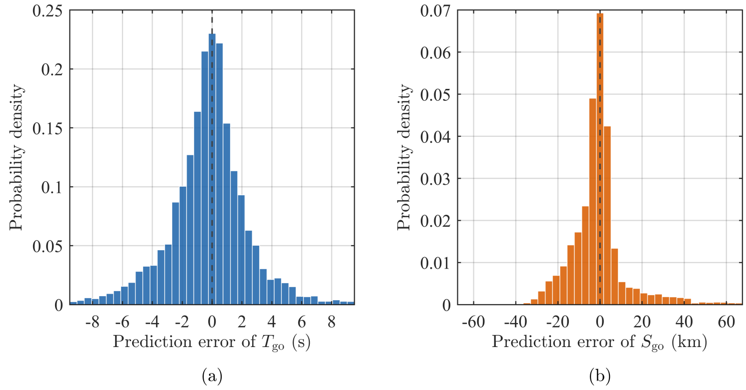

Fig. 3 Prediction error distributions of the proposed physics-informed predictor: (a) error of the remaining flight time; (b) error of the remaining flight range.

4.1.2 Ablation Study of Physics-Informed Loss

An ablation study was conducted to assess the contribution of each physics-informed loss component, as summarized in Table 2. The supervised-only model is the baseline. The other variants progressively add the range residual, the time-energy residual, and the slack variables. In the table, RMSE-T and RMSE-S denote the prediction RMSE of T_{go} and S_{go}. The quantities $\overline{|r_S|}$ and $\overline{|r_{TE}|}$ denote mean absolute residuals, while RMSE-r_S and RMSE-r_{TE} denote residual RMSE values.

Compared with the supervised-only model, the range-physics variant reduces RMSE-r_S from 0.5793 to 0.1935 and decreases RMSE-r_{TE} from 1.8214 to 0.7816. The time-energy variant reduces RMSE-r_{TE} to 0.0653 and lowers RMSE-r_S to 0.2392. Each physical constraint mainly improves its corresponding residual, while also affecting the other residual through the coupling between T_{go} and S_{go}.

When both physical residuals are imposed, the full physics-informed model without slack achieves a more balanced performance, reducing RMSE-T and RMSE-S to 2.276 s and 16.053, respectively, while keeping both residuals at low levels. This confirms the complementary roles of the range and time-energy constraints.

After slack variables are added, the full model gives the best prediction accuracy. RMSE-T and RMSE-S decrease to 2.203 s and 15.921 km, corresponding to reductions of about 7.9% and 3.2% relative to the supervised-only baseline. The values of $\overline{|r_S|}$ and RMSE-r_S decrease to 0.1171 and 0.1692, while $\overline{|r_{TE}|}$ and RMSE-r_{TE} decrease to 0.0331 and 0.0694. The time-energy-only variant gives a slightly smaller RMSE-r_{TE}, but it has larger prediction errors and a larger range residual. The full model with slack therefore gives the best trade-off between prediction accuracy and physical consistency for closed-loop predictor-corrector guidance.

Table 2 Ablation results of the physics-informed loss components.

Variant	Sup.	S	TE	Slack	RMSE-T	RMSE-S	$\overline{\lvert r_S \rvert}$	RMSE-S_r	$\overline{\lvert r_{TE} \rvert}$	RMSE-TE_r
Sup. only	✓	–	–	–	2.392	16.452	0.1442	0.5793	0.1081	1.8214
Range phy.	✓	✓	–	–	2.304	16.184	0.1257	0.1935	0.0752	0.7816
TE phy.	✓	–	✓	–	2.418	16.247	0.1314	0.2392	0.0341	**0.0653**
Full w/o slack	✓	✓	✓	–	2.276	16.053	0.1193	0.1764	0.0362	0.0735
Full phy. + slack	✓	✓	✓	✓	**2.203**	**15.921**	**0.1171**	**0.1692**	**0.0331**	0.0694

4.2 Nominal mission simulations

Nominal mission simulations are first used to assess the basic guidance behavior of the proposed longitudinal PINN-based predictor-corrector method. The numerical predictor-corrector guidance method is used as the baseline and is denoted as PCG. The proposed method, denoted as PINN-PCG, keeps the same correction framework but replaces numerical trajectory prediction with the trained physics-informed neural predictor. The simulation conditions are listed in Table 3. Three terminal-time-constrained cases are considered, with commanded terminal times of 1310, 1360, and 1400 s.

Table 3 Initial and terminal conditions for the single-HGV time-adjustability case

Item	h (km)	V (m/s)	λ (deg)	ϕ (deg)	ψ (deg)
Initial state	60.0	6000	1.0	4.0	90.0
Target state	23.5	1500	49.0	2.0	–

Figure 4 compares the ground tracks generated by PCG and PINN-PCG in the nominal cases. All trajectories converge to the prescribed target region, and the PINN-PCG tracks remain close to the PCG tracks. The neural predictor therefore preserves the basic closed-loop guidance behavior of the numerical predictor.

The altitude–velocity profiles in Fig. 5 reflect the different energy-management profiles required by the three terminal-time commands. In each case, the PINN-PCG profile remains close to the PCG profile, showing that the trained predictor provides correction information consistent with numerical propagation. The path-constraint histories in Fig. 6 show that heating rate, dynamic pressure, and load factor remain within their prescribed limits throughout flight. The terminal errors in Table 4 further show small terminal-time errors and acceptable range, altitude, and velocity errors for PINN-PCG in all nominal cases.

The single-step computational time was also recorded during the flight mission. One numerical-integration prediction required approximately 129.47 ms on average, whereas one neural-network prediction required approximately 1.44 ms. The neural predictor therefore used only 1.11% of the numerical-integration time. Replacing numerical propagation with a forward network evaluation substantially reduces the

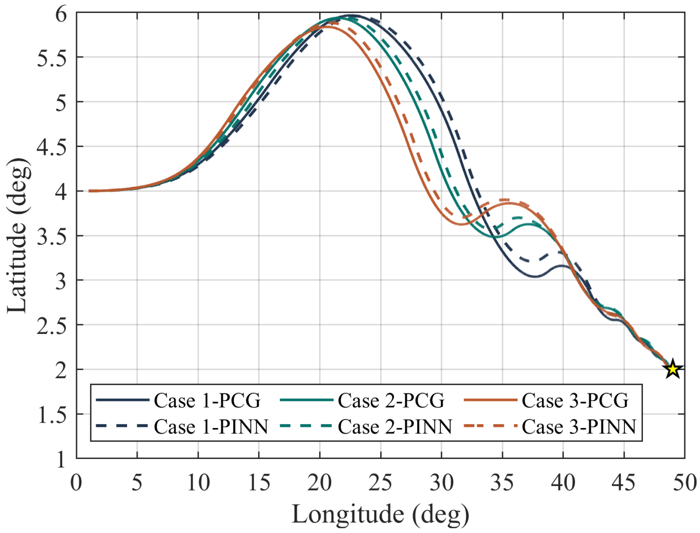

Fig. 4 Ground tracks in the nominal single-HGV time-adjustability simulations.

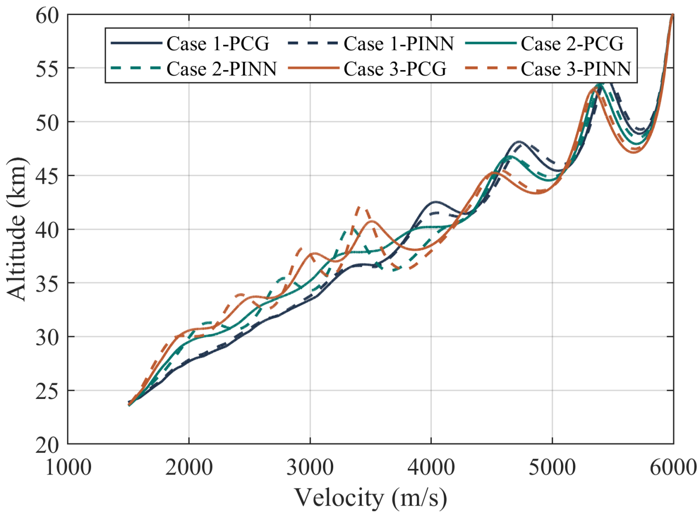

Fig. 5 Altitude–velocity profiles under different terminal-time commands.

online computational burden while preserving the time and range prediction needed for closed-loop correction.

The nominal simulations show that PINN-PCG maintains terminal-time control, terminal guidance accuracy, path-constraint satisfaction, and real-time prediction capability. This single-vehicle behavior provides the basis for the following cooperative guidance simulations.

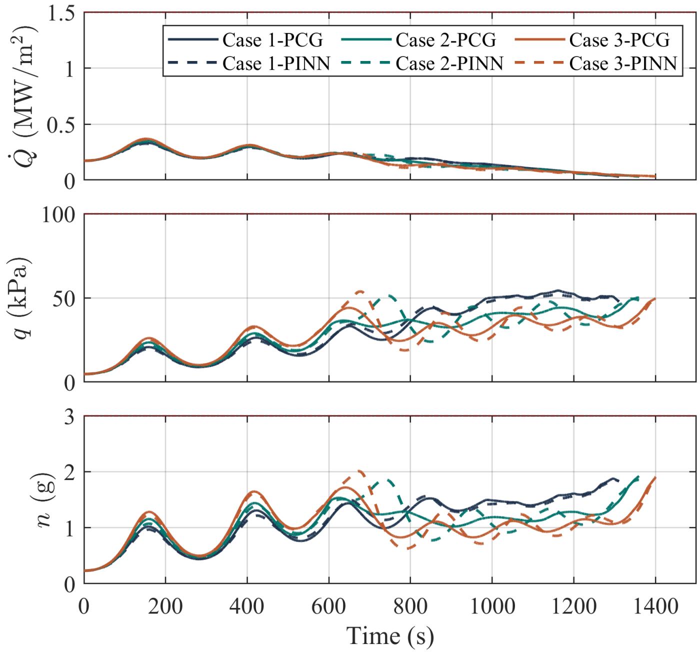

Fig. 6 Path-constraint histories in the nominal mission simulations.

Table 4 Terminal errors for the single-HGV time-adjustability validation

Method	t_{co} (s)	Δt (s)	ΔR (km)	Δh (m)	ΔV (m/s)
PCG	1310	0.831	5.096	390.099	-2.535
PINN-PCG	1310	0.616	4.615	378.714	-2.461
PCG	1360	-0.160	0.797	47.120	-0.306
PINN-PCG	1360	-0.204	1.430	273.702	-1.778
PCG	1400	0.561	1.052	122.484	-0.795
PINN-PCG	1400	0.523	1.539	83.079	-0.539

4.3 Multi-Vehicle Cooperative Guidance Simulations

After the single-vehicle time-adjustment capability is verified, multi-vehicle simulations are used to evaluate cooperative arrival-time control. The case includes five HGVs with different initial longitudes, latitudes, downrange distances, and heading angles, as summarized in Table 5. The terminal target is fixed at $(49°, 2°)$, and the cooperative arrival time is prescribed as $t_{\text{co}} = 1358$ s.

The cooperative ground tracks are shown in Fig. 7. Although the vehicles start from different lateral positions and heading angles, all trajectories converge to the same terminal region. The lateral separation decreases during flight, while the longitudinal channel regulates arrival time and remaining range.

Table 5 Initial conditions for the cooperative guidance case

Vehicle	h_0 (km)	V_0 (m/s)	λ_0 (deg)	ϕ_0 (deg)	R_0 (km)	ψ_0 (deg)
HGV-1	60.0	6000	2.018	-1.000	5233.944	83.336
HGV-2	60.5	5980	1.459	1.500	5283.945	86.662
HGV-3	59.5	6020	1.000	4.000	5333.945	90.913
HGV-4	60.2	6010	0.636	6.500	5383.945	95.103
HGV-5	59.8	5990	0.366	9.000	5433.945	99.245

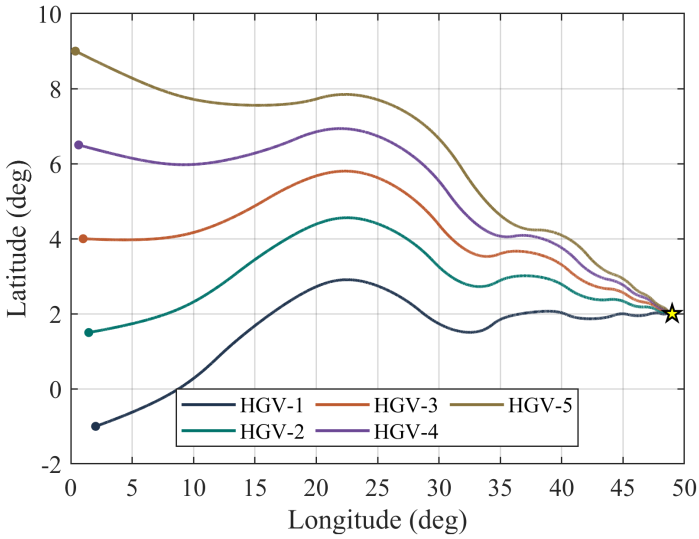

Fig. 7 Ground tracks of the cooperative guidance case.

The altitude and velocity histories in Fig. 8 show consistent energy-management trends across the five vehicles. The path-constraint histories in Fig. 9 show that heating rate, dynamic pressure, and normal load remain below their prescribed limits.

The terminal errors are summarized in Table 6. All vehicles satisfy the prescribed timing requirement. The largest absolute terminal-time error is 0.919 s, the maximum arrival-time dispersion is 0.852 s, and all range misses are below 5 km. Thus, PINN-PCG guides multiple HGVs with different initial states to the target region at nearly the same time in this cooperative case.

Table 6 Terminal errors of the cooperative guidance case

Vehicle	t_f (s)	Δt (s)	ΔR (km)	Δh (m)	ΔV (m/s)
HGV-1	1357.081	-0.919	4.210	1236.639	-8.048
HGV-2	1357.933	-0.067	1.715	537.415	-3.493
HGV-3	1357.855	-0.145	1.532	478.500	-3.109
HGV-4	1357.424	-0.576	1.286	-141.987	0.921
HGV-5	1357.836	-0.164	1.828	-46.366	0.301

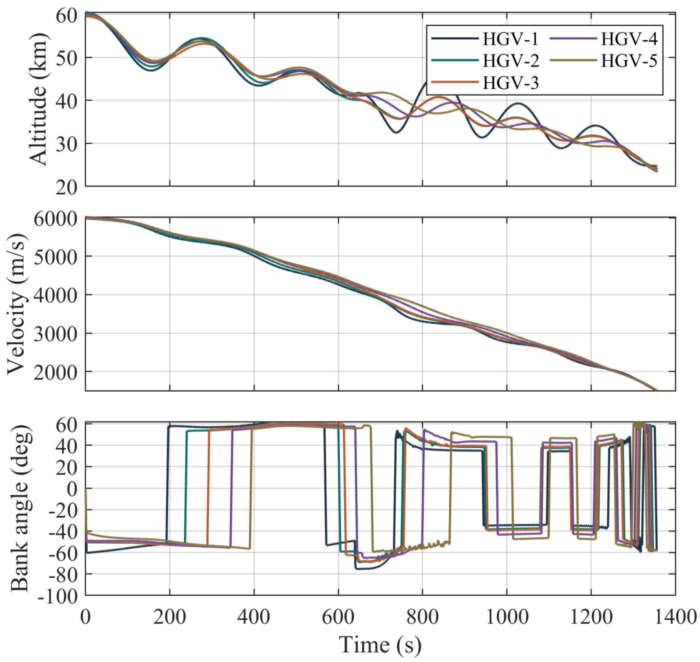

Fig. 8 State and control histories of the cooperative guidance case.

The multi-vehicle simulations show that PINN-PCG can coordinate arrival time without violating the major reentry path constraints. This conclusion is supported by the ground tracks, state histories, path-constraint histories, and terminal-error statistics. The validation is limited to the five-vehicle CAV-H setting considered here, so larger formations and stronger uncertainty cases remain open for further study.

4.4 Verification of Robustness of Cooperative Guidance Performance

To further verify the robustness of the cooperative guidance performance, a distribution-based validation was performed around the cooperative guidance case. The prescribed cooperative arrival time and terminal target were kept the same as those in Section 4.3. The validation contains 100 cooperative runs, and each run includes five HGVs, giving 500 vehicle-level terminal samples.

The vehicle-level error statistics are summarized in Table 7. The mean terminal height error is 989.318 m, with a standard deviation of 408.042 m and a maximum value of 2850.000 m. The mean absolute terminal velocity error is 6.439 m/s, and the maximum value is 18.640 m/s. The remaining range error has a mean value of 1.810 km and a maximum value of 4.850 km, remaining within the prescribed 5 km bound. The mean absolute arrival-time error is 0.405 s, and the maximum value is 1.618 s, which satisfies the 2 s timing requirement. These statistics indicate that the terminal state, remaining range, and cooperative timing errors remain bounded over the tested distribution.

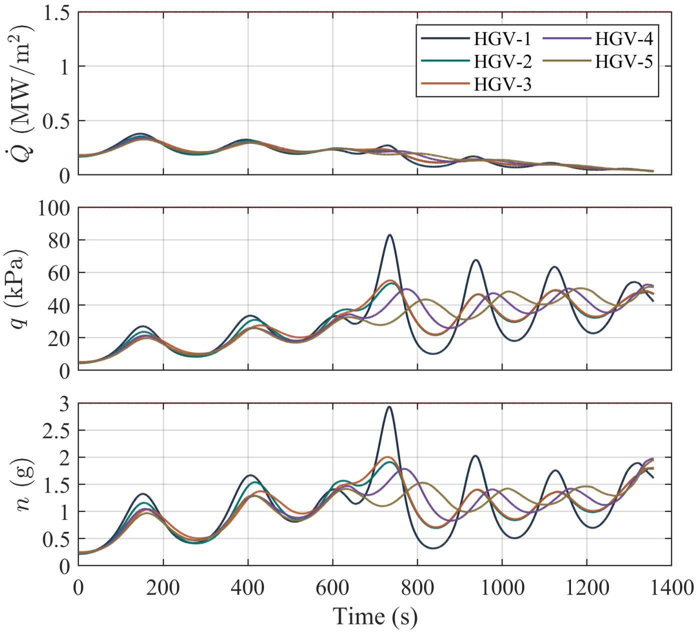

Fig. 9 Path-constraint histories of the cooperative guidance case.

Table 7 Vehicle-level terminal error statistics of the cooperative guidance case over MC simulations.

Metric	Mean	Max.	Std. dev.
Terminal height error Δh (m)	989.318	2850.000	408.042
Absolute terminal velocity error $\lvert\Delta V\rvert$ (m/s)	6.439	18.640	2.664
Remaining range error ΔR (km)	1.810	4.850	0.947
Absolute arrival-time error $\lvert\Delta t\rvert$ (s)	0.405	1.618	0.329

The distributions in Figs. 10 and 11 provide the corresponding run-level and terminal-state evidence. The five-HGV terminal-time span in Fig. 10(a) is concentrated near one second, and the terminal range miss in Fig. 10(b) remains below the 5 km requirement. The terminal altitude and velocity error distributions in Fig. 11(a) and (b) further show that the terminal energy state remains concentrated around the desired terminal condition. Therefore, the proposed PINN-PCG framework maintains cooperative timing, terminal-position accuracy, and terminal-state consistency under the tested robustness distribution.

5 Conclusion

This paper proposes a physics-informed neural predictor-corrector guidance method for time-coordinated reentry of multiple hypersonic glide vehicles. A longitudinal

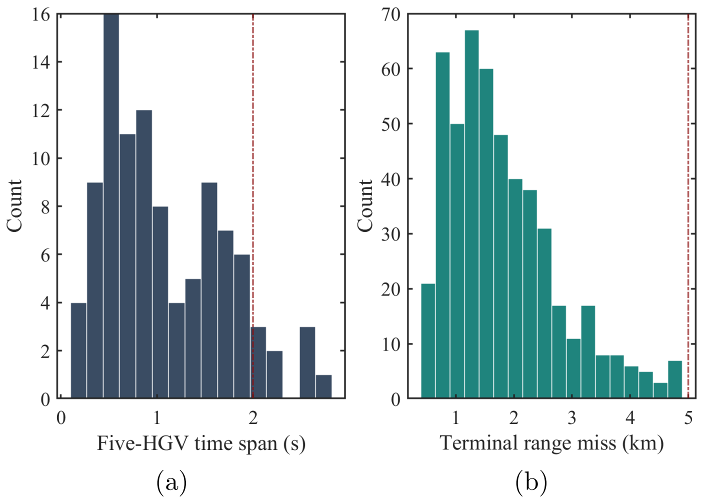

Fig. 10 Robustness distributions of cooperative terminal performance over MC simulations: (a) five-HGV terminal-time span within each cooperative run; (b) terminal range miss of the vehicle-level samples.

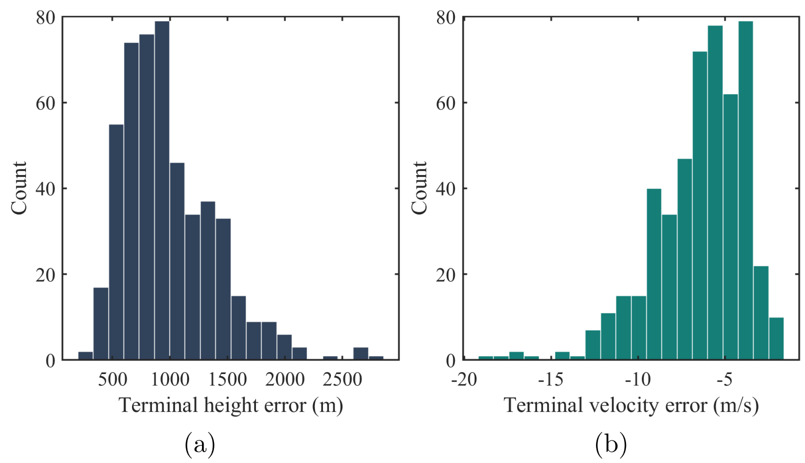

Fig. 11 Terminal-state error distributions over 500 vehicle-level samples: (a) terminal altitude error; (b) terminal velocity error.

predictor-corrector guidance framework is developed to regulate the remaining range and flight time through a two-parameter bank-angle magnitude profile. To reduce the online computational burden of conventional predictor-corrector guidance, a physics-informed neural predictor is embedded into the correction loop to estimate the time-to-go and range-to-go without repeated numerical trajectory propagation. Numerical simulations verify that the proposed PINN-PCG method can achieve accurate terminal-time control, improve computational efficiency, and maintain satisfactory guidance performance under uncertainties, demonstrating its effectiveness and robustness for multi-vehicle time-coordinated reentry missions.

Future work will focus on extending the proposed framework to larger-scale cooperative missions, stronger uncertainty environments, and more complex operational constraints, such as no-fly zones, communication limitations, and onboard implementation requirements. In addition, adaptive online updating of the physics-informed predictor may further improve guidance performance under model mismatch and uncertain aerodynamic conditions.

Declarations

- **Funding** Not applicable.

- **Conflict of interest** The authors have no relevant financial or non-financial interests to disclose.
- **Ethics approval** Not applicable.
- **Consent to participate** Not applicable.
- **Consent for publication** Not applicable.
- **Data availability** The data presented in this study are available on request from the corresponding author.
- **Materials availability** Not applicable.
- **Code availability** The code presented in this study is available on request from the corresponding author.
- **Author contributions** Not applicable.

References

[1] Lu, P., 2008. Predictor-corrector entry guidance for low-lifting vehicles. Journal of Guidance, Control, and Dynamics 31, 1067–1075.

[2] Xue, S., Lu, P., 2010. Constrained predictor-corrector entry guidance. Journal of Guidance, Control, and Dynamics 33, 1273–1281.

[3] Lu, P., 2014. Entry guidance: A unified method. Journal of Guidance, Control, and Dynamics 37, 713–728.

[4] Zeng, L., Zhang, H., Zheng, W., 2018. A three-dimensional predictor-corrector entry guidance based on reduced-order motion equations. Aerospace Science and Technology 73, 223–231.

[5] Liu, Z., Zheng, G., Zhang, B., Wei, J., Huang, H., 2024. Predictor-corrector reentry guidance for hypersonic glide vehicles based on high-precision analytical solutions. Aerospace Science and Technology 155, 109545.

[6] Li, Z., He, B., Wang, M., Lin, H., An, X., 2019. Time-coordination entry guidance for multi-hypersonic vehicles. Aerospace Science and Technology 89, 123–135.

[7] Guo, Y., Li, X., Zhang, H., 2020. Entry guidance with terminal time control based on quasi-equilibrium glide condition. IEEE Transactions on Aerospace and Electronic Systems 56, 887–896.

[8] Wang, H., Guo, J., Wang, X., 2022. Time-coordination entry guidance using a range-determined strategy. Aerospace Science and Technology 129, 107842.

[9] Liang, Z., Lv, C., Zhu, S., 2023. Lateral entry guidance with terminal time constraint. IEEE Transactions on Aerospace and Electronic Systems 59, 2544–2553.

[10] Shi, P., Xu, J., Cheng, L., Dong, C., Huang, X., 2025. Real-time lateral predictor-corrector entry guidance with terminal heading angle constraint. IEEE Transactions on Aerospace and Electronic Systems 61, 2106–2119.

[11] Yang, H., Liang, H., Liu, J., 2024. Analytical time-coordinated entry guidance for multi-hypersonic vehicles within three-dimensional corridor. Aerospace Science and Technology 155, 109639.

[12] Liu, X., Li, X., Zhang, H., 2025. Entry guidance with terminal time constraint based on reduced-order dynamics. IEEE Transactions on Aerospace and Electronic Systems 61, 5949–5961.

[13] Yu, W., Chen, W., Jiang, Z., Zhang, W., Zhao, P., 2019. Analytical entry guidance for coordinated flight with multiple no-fly-zone constraints. Aerospace Science and Technology 84, 273–290.

[14] Zhao, K., Song, J., Liu, Y., 2025. Spatial-temporal cooperative guidance with no-fly zones avoidance. Control Engineering Practice 154, 106162.

[15] Cheng, L., Jiang, F., Wang, Z., 2021. Multiconstrained real-time entry guidance using deep neural networks. IEEE Transactions on Aerospace and Electronic Systems 57, 325–340.

[16] Li, Z., Guo, J., Tang, S., Ji, S., 2023. A deep learning-based approach to time-coordination entry guidance for multiple hypersonic vehicles. The Aeronautical Journal 127, 604–626.

[17] Jiang, L., Nan, Y., Zhang, Y., Li, Z., Zhang, J., 2022. Anti-interception guidance for hypersonic glide vehicle: A deep reinforcement learning approach. Aerospace 9, 424.

[18] Su, L., Wang, J., Chen, H., 2023. A real-time and optimal hypersonic entry guidance method using inverse reinforcement learning. Aerospace 10, 948.

[19] Li, X., Wang, X., Zhou, H., 2024. Entry guidance for spatial no-fly zones avoidance via model-based reinforcement learning. Aerospace Science and Technology 153, 109405.

[20] Bartusiak, E.R., Jacobs, M.A., Chan, M., Comer, M.L., Delp, E.J., 2024. Predicting hypersonic glide vehicle behavior with stochastic grammars. IEEE Transactions on Aerospace and Electronic Systems 60, 1208–1223.

[21] Brunton, S.L., Noack, B.R., Koumoutsakos, P., 2020. Machine learning for fluid mechanics. Annual Review of Fluid Mechanics 52, 477–508.

[22] Raissi, M., Perdikaris, P., Karniadakis, G.E., 2019. Physics-informed neural networks: A deep learning framework for solving forward and inverse problems involving nonlinear partial differential equations. Journal of Computational Physics 378, 686–707.

[23] Karniadakis, G.E., Kevrekidis, I.G., Lu, L., Perdikaris, P., Wang, S., Yang, L., 2021. Physics-informed machine learning. Nature Reviews Physics 3, 422–440.

[24] Willard, J., Jia, X., Xu, S., Steinbach, M., Kumar, V., 2022. Integrating scientific knowledge with machine learning for engineering and environmental systems. ACM Computing Surveys 55, 1–37.

[25] Jagtap, A.D., Kharazmi, E., Karniadakis, G.E., 2020. Conservative physics-informed neural networks on discrete domains for conservation laws: Applications to forward and inverse problems. Computer Methods in Applied Mechanics and Engineering 365, 113028.

[26] Cuomo, S., Di Cola, V.S., Giampaolo, F., Rozza, G., Raissi, M., Piccialli, F., 2022. Scientific machine learning through physics-informed neural networks: Where we are and what's next. Journal of Scientific Computing 92, 88.

[27] Lu, L., Meng, X., Mao, Z., Karniadakis, G.E., 2021a. DeepXDE: A deep learning library for solving differential equations. SIAM Review 63, 208–228.

[28] Lu, L., Jin, P., Pang, G., Zhang, Z., Karniadakis, G.E., 2021b. Learning nonlinear operators via DeepONet based on the universal approximation theorem of operators. Nature Machine Intelligence 3, 218–229.

[29] Mao, Z., Jagtap, A.D., Karniadakis, G.E., 2020. Physics-informed neural networks for high-speed flows. Computer Methods in Applied Mechanics and Engineering 360, 112789.

[30] Wang, S., Teng, Y., Perdikaris, P., 2021. Understanding and mitigating gradient flow pathologies in physics-informed neural networks. SIAM Journal on Scientific Computing 43, A3055–A3081.

[31] Wang, S., Yu, X., Perdikaris, P., 2022. When and why PINNs fail to train: A neural tangent kernel perspective. Journal of Computational Physics 449, 110768.

[32] Yu, J., Lu, L., Meng, X., Karniadakis, G.E., 2022. Gradient-enhanced physics-informed neural networks for forward and inverse PDE problems. Computer Methods in Applied Mechanics and Engineering 393, 114823.

[33] McClenny, L.D., Braga-Neto, U.M., 2023. Self-adaptive physics-informed neural networks. Journal of Computational Physics 474, 111722.

[34] Wu, C., Zhu, M., Tan, Q., Kartha, Y., Lu, L., 2023. A comprehensive study of non-adaptive and residual-based adaptive sampling for physics-informed neural networks. Computer Methods in Applied Mechanics and Engineering 403, 115671.

[35] Wang, S., Sankaran, S., Perdikaris, P., 2024. Respecting causality for training physics-informed neural networks. Computer Methods in Applied Mechanics and Engineering 421, 116813.

[36] Xu, H., Cai, G., Fan, Y., Wei, H., Li, X., 2023. Analytic time reentry cooperative guidance for multi-hypersonic glide vehicles. Applied Sciences 13, 4987.